Inorganic Chemistry
ARTICLE
pubs.acs.org/IC

Syntheses, Electronic Structures, and EPR/UV−Vis−NIR Spectroelectrochemistry of Nickel(II), Copper(II), and Zinc(II) Complexes with a Tetradentate Ligand Based on S-Methylisothiosemicarbazide

Vladimir B. Arion,*[†] Peter Rapta,*[‡] Joshua Telser,*[§] Sergiu S. Shova,[∥,⊥] Martin Breza,[‡] Karol Lušpai,[‡] and Jozef Kožišek[‡]

[†]Institute of Inorganic Chemistry, University of Vienna, Währinger Strasse 42, A-1090 Vienna, Austria

[‡]Department of Physical Chemistry, Slovak University of Technology, Radlinského 9, SK-81237 Bratislava, Slovak Republic

[§]Department of Biological, Chemical and Physical Sciences, Roosevelt University, 430 S Michigan Avenue, Chicago, Illinois 60605, United States

[∥]Department of Chemistry, Moldova State University, A. Mateevici Street 60, Chişinău, Moldova

[⊥]"Petru Poni" Institute of Macromolecular Chemistry, Aleea Grigore Ghica Vodă 41A, RO-700487 Iaşi, Romania

Supporting Information

ABSTRACT: Template condensation of 3,5-di-*tert*-butyl-2-hydroxybenzaldehyde S-methylisothiosemicarbazone with pentane-2,4-dione and triethyl orthoformate at elevated temperatures resulted in metal complexes of the type $M^{II}L$, where M = Ni and Cu and H_2L = a novel tetradentate ligand. These complexes are relevant to the active site of the copper enzymes galactose oxidase and glyoxal oxidase. Demetalation of $Ni^{II}L$ with gaseous hydrogen chloride in chloroform afforded the metal-free ligand H_2L. Then by the reaction of H_2L with $Zn(CH_3COO)_2 \cdot 2H_2O$ in a 1:1 molar ratio in 1:2 chloroform/methanol, the complex $Zn^{II}L(CH_3OH)$ was prepared. The three metal complexes and the prepared ligand were characterized by spectroscopic methods (IR, UV−vis, and NMR spectroscopy), X-ray crystallography, and DFT calculations. Electrochemically generated one-electron oxidized metal complexes $[NiL]^+$, $[CuL]^+$, and $[ZnL(CH_3OH)]^+$ and the metal-free ligand cation radical $[H_2L]^{+\bullet}$ were studied by EPR/UV−vis−NIR and DFT calculations. These studies demonstrated the interaction between the metal ion and the phenoxyl radical.

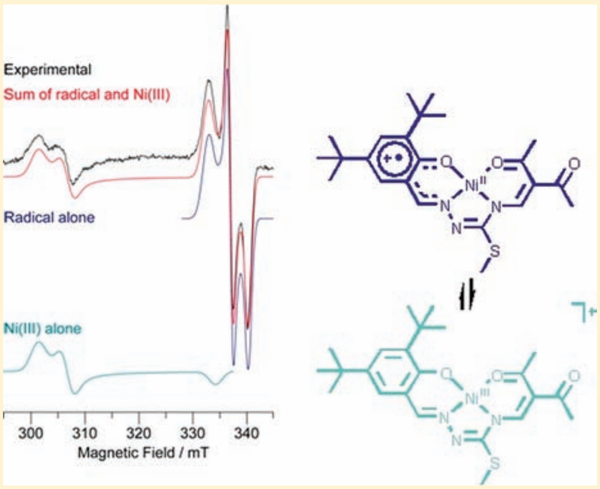

INTRODUCTION

Interest in the coordination chemistry of phenoxyl radicals was triggered by the full characterization of the active sites of galactose oxidase (GAO) and glyoxal oxidase (GLO) using protein X-ray crystallography.[1,2] Each active site consists of a mononuclear copper(II) and a tyrosyl radical. Another interesting structural attribute is the presence of a thioether bond linking Cys228 and Tyr278 in GAO. These two metalloenzymes perform two-electron oxidation of primary alcohols to aldehydes and oxidation of aldehydes to carboxylic acids, respectively, with concomitant conversion of O_2 to H_2O_2. Efforts made by several groups on the synthesis of metal phenoxyl radical complexes to model the active site in these biological systems in terms of spectral properties, structural features, and reactivity have been reviewed.[3−6] Although impressive progress has been achieved, there are still intriguing issues remaining mainly related to the enzymes' active site electronic structure,[5] which stimulate further activity in this fascinating field of research.

A number of bis(phenolate)copper(II) complexes which can reproduce the spectral features and reactivity of GAO have been prepared by using substituted salen, reduced salen-type, and other Schiff-base ligand frames (shown in Chart 1).[3−10] All mononucleating systems in Chart 1 contain two protected phenolate units and can potentially produce two phenoxyl radicals upon two sequential one-electron oxidations. Examples of dinucleating and trinucleating systems containing phenolate moieties are rare (Chart 2).[11,12] The use of metal ions rather than

Received: November 12, 2010
Published: March 01, 2011

ACS Publications © 2011 American Chemical Society

Chart 1

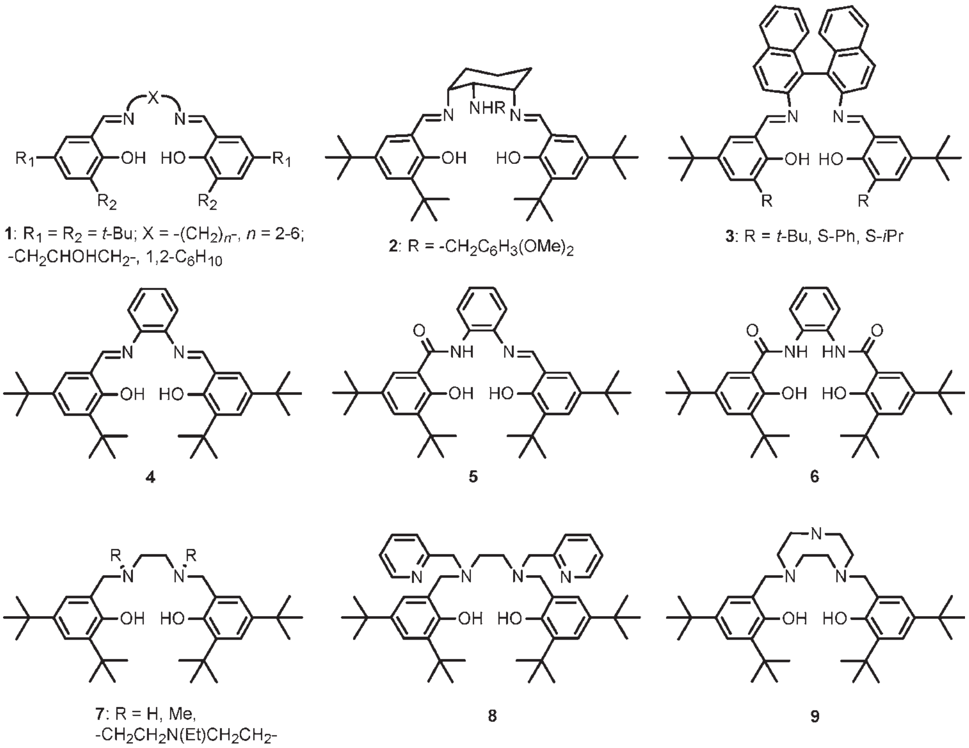

1: $R_1 = R_2 = t$-Bu; X = $-(CH_2)_n-$, n = 2-6; $-CH_2CHOHCH_2-$, 1,2-C_6H_{10}

2: R = $-CH_2C_6H_3(OMe)_2$

3: R = t-Bu, S-Ph, S-iPr

4

5

6

7: R = H, Me, $-CH_2CH_2N(Et)CH_2CH_2-$

8

9

Chart 2

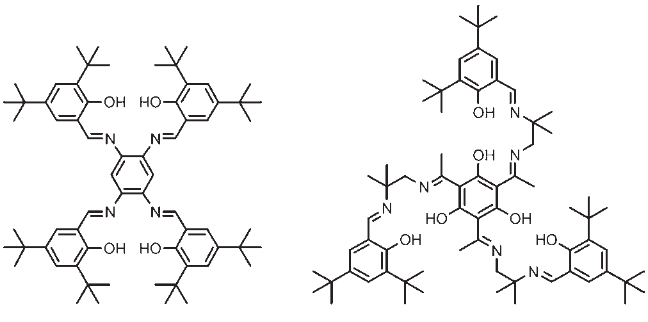

10

11

copper(II), e.g., nickel(II), cobalt(II), or zinc(II),[13−15] is another dimension emerging in this research area, which can lead to the creation of novel synthetic catalysts for selective oxidation reactions. Some of these complexes can be chemically or electrochemically oxidized by one electron to give products which exhibit temperature- or ligand field geometry-dependent valence tautomerism between a higher-valent metal−phenolate and a metal−phenoxyl radical (i.e., $[M^{n+}-(PhO^-)]^{(n-1)+}$ vs $[M^{(n-1)+}-(PhO^\bullet)]^{(n-1)+}$).[12,16−18] Since phenoxyl radicals are transient, sometimes elusive species, bulky protecting groups have been introduced into the ortho and para positions of the parent phenol moiety to stabilize the radical formation and protect it from further bis(μ-phenolate) dimerization.[5,19] The first crystal structure of a monomeric metal-free 2,4,6-tri-*tert*-butylphenoxyl radical, a very convenient reagent for hydrogen atom transfer studies, has been recently reported.[20] Additional stabilization of phenoxyl radicals can be realized via hydrogen bonding or metal coordination by exploiting suitable supporting ligand frames.[21] Introduction of space-demanding substituents induce, in addition, tetrahedral distortion of square-planar salen-type N_2O_2 coordination geometry, which is important for stabilizing Cu(I) in this coordination environment.[5] The extent of this distortion can be increased by using large (3 and more atoms) spacers between salicylidene moieties, as shown in **1**. Other coordination geometries were adopted when reduced salen-type ligands containing additional dangling picolyl groups were used for the generation of stable metal-phenoxyl radicals, as shown in **8**. The ligand **9** based on triazacyclononane[22] can also be regarded as a reduced salen-type system.

Herein, we report on the synthesis of a new ligand, H_2L, with a N_2O_2 donor set (Scheme 1), which contains a single phenolate moiety, suitably protected by bulky *tert*-butyl substituents in the ortho and para positions of the parent phenol, which enable the ligand to form a phenoxyl radical that is detectable at room temperature and contains a thiomethyl group attached to the extended π-conjugated system of the ligand frame. The effects of nickel(II), copper(II), and zinc(II) on the electrochemically generated phenoxyl radical are explored in this work.

■ EXPERIMENTAL SECTION

Starting Materials. 3,5-Di-*tert*-butyl-2-hydroxybenzaldehyde and $Cu(acac)_2$ were purchased from Aldrich. S-Methylisothiosemicarbazide hydroiodide was synthesized by following the literature procedure.[23] 3,5-Di-*tert*-butyl-2-hydroxybenzaldehyde S-methylisothiosemicarbazone was prepared using a condensation reaction of equimolar amounts of 3,5-di-*tert*-butyl-2-hydroxybenzaldehyde and S-methylisothiosemicarbazide hydroiodide in 1:1 EtOH/H_2O followed by the addition of equivalent amount of Na_2CO_3. Acetamidrazone hydrochloride was prepared as described in the literature.[24] A condensation reaction

Scheme 1. Synthetic Pathway to H_2L and Metal Complexes Prepared in This Work[a]

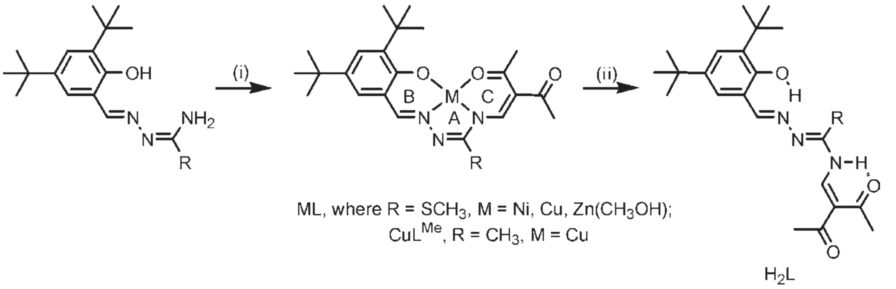

[a] Reagents and conditions: (i) $M(acac)_2$ (M = Ni, Cu), Hacac (Hacac = pentane-2,4-dione), $CH(OC_2H_5)_3$, 105 °C, 8−16 h; (ii) $CHCl_3$, HCl_g. $ZnL(CH_3OH)$ was prepared from zinc(II) acetate and H_2L.

between 3,5-di-*tert*-butyl-2-hydroxybenzaldehyde and acetamidrazone hydrochloride in ethanol/water 2:1 in the presence of an equimolar amount of Na_2CO_3 afforded a Schiff base. $Ni(acac)_2 \cdot 2H_2O$ was prepared by following the procedure reported for $Zn(acac)_2 \cdot H_2O$[25] and dehydrated by heating it in vacuo at 90 °C for 12 h. Pentane-2,4-dione and triethyl orthoformate were obtained from Aldrich and distilled before use. Dichloromethane (p.a.) and tetra-*n*-butylammonium hexafluorophosphate ($TBAPF_6$, p.), both purchased from Fluka, and ferrocene (98.0%) purchased from Merck were used as received.

Synthesis of the Metal(II) Complexes and the Metal-Free Ligand. *Ni^{II}L.* A suspension of 3,5-di-*tert*-butyl-2-hydroxybenzaldehyde S-methylisothiosemicarbazone (2.50 g, 7.0 mmol) and $Ni(acac)_2$ (1.8 g, 7.0 mmol) in pentane-2,4-dione (24 mL) and triethyl orthoformate (6 mL) was heated under an argon atmosphere at 107 °C for 8 h. The reaction mixture was allowed to cool to room temperature. The precipitate formed was filtered off, washed with ethanol and diethyl ether, and dried in the air. Yield: 1.20 g, 34.6%. Calcd for $C_{23}H_{31}NiN_3O_3S \cdot 0.5H_2O$ (M_r 496.15 g/mol), %: C, 55.63; H, 6.50; N, 8.47; S, 6.44. Found, %: C, 55.75; H, 6.41; N, 8.60; S, 6.36. ^1H NMR (500.10 MHz, $CDCl_3$): δ 8.09 (s, 1H, CH=N), 7.96 (s, 1H, =CH−N), 7.42 (s, 1H, Ar), 7.10 (s, 1H, Ar), 2.70 (s, 3H, CH_3), 2.63 (s, 3H, CH_3), 2.42 (s, 3H, CH_3), 1.44 (s, 9H, $C(CH_3)_3$), 1.31 (s, 9H, $C(CH_3)_3$). IR spectrum (ATR, selected bands, ν_{max}): 1656, 1584, 1532, 1296, 1170, 942, 783, 622 cm^{-1}. UV−vis in CH_2Cl_2, λ, nm (ε, M^{-1} cm^{-1}): 472 (8440), 401 (20610), 371 (20690), 317 (19675), 293 (25365), 257 (51030).

Cu^{II}L. A suspension of 3,5-di-*tert*-butyl-2-hydroxybenzaldehyde S-methylisothiosemicarbazone (1.42 g, 4.0 mmol) and $Cu(acac)_2$ (1.0 g, 3.8 mmol) in pentane-2,4-dione (12 mL) and triethyl orthoformate (3 mL) was heated under an argon atmosphere at 107 °C for 16 h. The reaction mixture was allowed to cool to room temperature. The precipitate formed was filtered off, washed with ethanol and diethyl ether, and dried in the air. The crude product, contaminated with $Cu(acac)_2$, was dissolved in chloroform and reprecipitated with ethanol. Yield: 0.66 g, 35.3%. Calcd for $C_{23}H_{31}CuN_3O_3S$ (M_r 492.14 g/mol), %: C, 56.08; H, 6.35; N, 8.54; S, 6.50. Found, %: C, 55.74; H, 6.43; N, 8.59; S, 6.36. IR spectrum, (ATR, selected bands, ν_{max}): 1657, 1583, 1525, 1462, 1362, 1289, 1167, 939, 786, 607 cm^{-1}. UV−vis in CH_2Cl_2, λ, nm (ε, $M^{-1}cm^{-1}$): 445 (10200), 374 (19525), 362 (20630), 315 (21030), 305 (20870), 284 (19205), 255 (31650).

H$_2$L. Hydrogen chloride was bubbled through a solution of NiL (0.27 g, 0.55 mmol) in chloroform (50 mL). The red color of the solution faded gradually, and it became light-yellow. Water (200 mL) was added, and after vigorous stirring, the organic layer was separated from the aqueous phase using a separating funnel. This operation was repeated 5−6 times to ensure the removal of nickel(II) from the organic layer. The chloroform was evaporated under reduced pressure almost to dryness, and to the remaining residue was added ethanol (10−12 mL). The solution was allowed to stand at 4 °C overnight. The crystals formed were separated by filtration and washed with cold ethanol (5 mL). The crystallized product was also suitable for X-ray diffraction measurement. Yield: 0.19 g, 76.9%. Mp 169−170 °C. Calcd for $C_{23}H_{34.2}N_3O_{3.6}S$ (M_r 442.40 g/mol), %: C, 62.44; H, 7.79; N, 9.50; S, 7.25. Found, %: C, 62.25; H, 7.76; N, 9.32; S, 7.10. ESI-MS (CH_3OH) positive: m/z 432 $[M + H]^+$, 454 $[M + Na]^+$; negative: m/z 430 $[M - H^+]^-$. UV−vis in CH_2Cl_2, λ, nm (ε, $M^{-1}cm^{-1}$): 381 (41120), 348 (29105), 291 (21455).

Zn^{II}L·CH$_3$OH. To H_2L (108 mg, 0.25 mmol) in chloroform (3 mL) was added $Zn(CH_3COO)_2 \cdot 2H_2O$ (55 mg, 0.25 mmol) in methanol (6 mL). After 24 h, the crystals formed were filtered off, washed with methanol, and dried in the air. Yield: 72 mg, 54.8%. Calcd for $C_{24}H_{35}N_3O_4SZn$ (M_r 525.16 g/mol), %: C, 54.70; H, 6.69; N, 7.97; S, 6.08. Found, %: C, 54.25; H, 6.77; N, 7.84; S, 6.04. ^1H NMR (500.10 MHz, DMSO-d_6): δ = 8.57 (s, 1H, CH=N), 8.56 (s, 1H, =CH−N), 7.28 (d, 1H, Ar), 7.13 (d, 1H, Ar), 4.10 (q, 1H, CH_3OH), 3.18 (d, 3H, CH_3OH), 2.56 (s, 3H, CH_3), 2.49 (s, 3H, CH_3), 2.33 (s, 3H, CH_3), 1.46 (s, 9H, $C(CH_3)_3$), 1.26 (s, 9H, $C(CH_3)_3$). UV−vis in CH_2Cl_2, λ, nm (ε, M^{-1} cm^{-1}): 437 (8770), 351 (19745), 303 (23080), 250 (18040). The quality of the crystals was suitable for X-ray diffraction analysis.

Cu^{II}L^{Me}·0.6H$_2$O. A suspension of a Schiff base of 3,5-di-*tert*-butyl-2-hydroxybenzaldehyde and acetamidrazone (1.00 g, 3.5 mmol) and $Cu(acac)_2$ (0.6 g, 2.3 mmol) in pentane-2,4-dione (8 mL) and triethyl orthoformate (2 mL) was heated under an argon atmosphere at 107 °C for 20 h. The reaction mixture was allowed to cool to ca. 50 °C and filtered. The filtrate was cooled slowly and allowed to stand at 4 °C for 24 h. The crystallized product was filtered off and washed with ethanol. The orange well-shaped crystals suitable for X-ray diffraction were contaminated with $Cu(acac)_2$. Therefore, the product was purified by column chromatography on silica by using CH_2Cl_2 as an eluent. Yield: 0.09 g, 8.3%. Calcd for $C_{23}H_{32.2}CuN_3O_{3.6}$ (M_r 471.87 g/mol), %: C, 58.54; H, 6.88; N, 8.91. Found, %: C, 58.25; H, 6.77; N, 8.89.

Analytical and Spectroscopic Measurements. ^1H NMR spectra were recorded at 298 K on a Bruker FT NMR spectrometer, Avance III 500 MHz, at an operating frequency of 500.10 MHz. The C, H, N, and S elemental analyses were performed by the Laboratory for Elemental Analysis, Faculty of Chemistry, University of Vienna, by using a Perkin-Elmer 2400 CHN Elemental Analyzer. IR spectra were measured on a Bruker Vertex 70 FT-IR-spectrometer by means of attenuated total reflection (ATR) techniques. Electrospray ionization mass spectrometry (ESI-MS) measurements were carried out with a Bruker Esquire 3000 instrument; the samples were dissolved in methanol. Electronic absorption spectra of compounds dissolved in CH_2Cl_2 were recorded at room temperature with a Perkin-Elmer Lambda 650 spectrophotometer between 240 and 900 nm or PC2000 (Ocean Optics, Inc.). All cyclovoltammetric experiments were performed at room temperature under a nitrogen atmosphere. A standard three electrode arrangement of a platinum wire as the working electrode, a platinum wire

Table 1. Crystal Data and Details of Data Collection for NiL, CuL, ZnL(CH_3OH), H_2L, and CuL^{Me}

compound	NiL	CuL	ZnL(CH_3OH)	H_2L	CuL^{Me}
empirical formula	$C_{23}H_{31}NiN_3O_3S$	$C_{23}H_{31}CuN_3O_3S$	$C_{24}H_{34}ZnN_3O_4S$	$C_{23}H_{33}N_3O_3S$	$C_{23}H_{31}CuN_3O_3$
fw	488.28	493.11	525.97	431.58	461.05
space group	$P2_1/c$	*Pnma*	$P2_1/n$	$P\bar{1}$	$C2/c$
a [Å]	32.3176(19)	31.637(6)	10.4094(4)	10.0352(13)	34.687(3)
b [Å]	7.2509(3)	6.9058(14)	9.2257(4)	14.3427(16)	13.8621(11)
c [Å]	21.5531(10)	10.956(2)	27.7560(10)	17.316(2)	9.5329(6)
α [deg]				78.711(7)	
β [deg]	109.426(3)		97.096(2)	79.905(7)	93.060(7)
γ [deg]				87.707(7)	
V [Å^3]	4763.1(4)	2393.6(8)	2645.10(18)	2406.2(5)	4577.2(6)
Z	8	4	4	4	8
λ [Å]	0.71073	0.71073	0.71073	0.71073	0.71073
ρ_{calcd} [g cm^{-3}]	1.362	1.368	1.321	1.191	1.338
cryst size [mm^3]	0.80 × 0.20 × 0.04	0.50 × 0.05 × 0.01	0.25 × 0.10 × 0.06	0.98 × 0.33 × 0.16	0.22 × 0.22 × 0.08
T [K]	100	100	100	100	100
μ [mm^{-1}]	0.931	1.028	1.040	0.162	0.982
R_1[a]	0.0669	0.0382	0.0433	0.0665	0.0595
wR_2[b]	0.1585	0.0887	0.0990	0.0986	0.1668
GOF[c]	1.010	1.038	1.069	0.962	1.018

[a] $R_1 = \Sigma||F_o| - |F_c||/\Sigma|F_o|$. [b] $wR_2 = \{\Sigma[w(F_o^2 - F_c^2)^2]/\Sigma[w(F_o^2)^2]\}^{1/2}$. [c] GOF $= \{\Sigma[w(F_o^2 - F_c^2)^2]/(n - p)\}^{1/2}$, where n is the number of reflections, and p is the total number of parameters refined.

as the counter electrode, and a silver wire as the pseudoreference electrode was used. The recorded oxidation potentials were obtained with a scan rate of 0.10 V s^{-1}. Sample solutions with an approximate concentration of 0.5 mM, prepared with 0.2 M $TBAPF_6$ supporting electrolyte in CH_2Cl_2, were purged with N_2 for 5 min before each experiment. The electrochemical measurements were carried out with a HEKA PG 284 (Lambrecht, Germany) potentiostat/galvanostat using the PotPulse 8.53 software package. Ferrocene (Fc) was used as an internal standard. Electrochemical oxidation of the investigated compounds with simultaneous UV−vis and EPR measurements was carried out in a Varian flat spectroelectrochemical cell using platinum mesh as a working electrode. Platinum wire served as a counter electrode, and a silver wire calibrated against the Fc/Fc^+ redox-couple served as a pseudoreference electrode. The cell was filled and tightly closed, and in situ spectroelectrochemical experiments were performed in the optical EPR cavity (ER4104OR, Bruker, Germany). The EPR spectra were recorded on different spectrometers: for X-band, both an EMX EPR spectrometer (Bruker, Germany) and a modified Varian E-4 spectrometer (Chicago); for Q-band (35 GHz), a modified Varian E-109 spectrometer was used.[26] The Q-band spectrometer employs a liquid He immersion dewar so that spectra are recorded at 2 K under "passage" conditions which yield an absorption line shape; a digital derivative spectrum is shown for easier comparison with conventional EPR spectral presentation. EPR simulations employed the Bruker software WinSim and the program QPOW, by R. L. Belford, as modified by J. Telser. In situ UV−vis−NIR spectroelectrochemistry of $M^{II}L$ complexes was performed in a 0.2 M $TBAPF_6$ solution in CH_2Cl_2 using a double-beam Shimadzu 3600 spectrometer. The working electrode was placed in a 1 mm optical cell with Pt auxiliary and Ag-wire pseudoreference electrodes. EPR spectra of $[NiL]^+$ (one electron oxidized $Ni^{II}L$) on a Pt-mesh electrode at 77 K were recorded ex situ after a certain potential, controlled by the HEKA PG 284 potentiostat, was applied for 60 s with immediate immersion into liquid nitrogen after the application of a potential step. The electrode contacts to the potentiostat were removed after cooling. A standard EPR tube cell (3 mm diameter) was used with Ag wire as a pseudoreference electrode and Pt-mesh as a counter electrode.

Crystallographic Structure Determination. X-ray diffraction measurements were performed with a Bruker X8 APEX II CCD diffractometer at 100 K. Single crystals were positioned at 35, 50, 35, 35, and 35 mm from the detector, and 1917, 2488, 1961, 1211, and 1075 frames were measured, each for 30, 30, 30, 60, and 70 s over 0.5, 1, 1, 1, and 1° scan widths for NiL, CuL, ZnL(CH_3OH), H_2L, and CuL^{Me}, respectively. The data were processed using the SAINT software package.[27] Crystal data, data collection parameters, and structure refinement details are given in Table 1. The structures were solved by direct methods and refined by full-matrix least-squares techniques. Non-hydrogen atoms were refined with anisotropic displacement parameters. H atoms were placed at calculated positions and refined as riding atoms in the subsequent least-squares model refinements. The isotropic thermal parameters were estimated to be 1.2 times the values of the equivalent isotropic thermal parameters of the non-hydrogen atoms to which hydrogen atoms were bonded. SHELXS-97 was used for structure solution and SHELXL-97 for refinement;[28] molecular diagrams were produced with ORTEP.[29] Refinement of the structures revealed that acetyl and both $-C(CH_3)_3$ groups in CuL occupy two statistically disordered positions on the opposite sides of the planar molecule with 50% probability. In CuL^{Me}, only one $-C(CH_3)_3$ group is statistically disordered with a 50% probability. The same approach, in combination with the available tools (PART, DFIX, and SADI) of SHELXL97, was used for NiL because of the disorder in one of the $-C(CH_3)_3$ groups of the ligand. The fractional contributions of the two positions are in 0.4:0.6 and 0.7:0.3 ratios, for A and B molecules, respectively.

DFT Calculations. The geometries of the transition metal complexes $M^{II}L$ (M = Ni, Cu, Zn) and the ligand H_2L as well as of one-electron oxidized species $[ML]^+$ (M = Ni, Cu, Zn) and $[H_2L]^{+\bullet}$ were optimized at the B3LYP level of theory (starting from experimental X-ray structures of $Ni^{II}L$, $Cu^{II}L$, $Zn^{II}L(CH_3OH)$, and H_2L) without any symmetry restrictions using the Gaussian 03 program package.[30] The standard 6-311G* basis set has been used for transition metal, sulfur, oxygen, and nitrogen atoms and the 6-31G* one for the remaining atoms (basis I). The stability of the obtained structures has been tested by vibrational analysis (no imaginary vibrations). On the basis of the optimized B3LYP geometries, the vertical transition energies and oscillator strengths between the initial and final electron states for electronic absorption spectra (up to 120 excited states) were computed

Chart 3

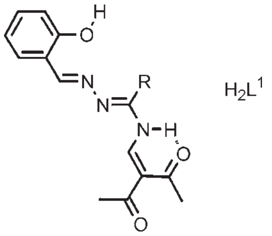

by the TD-DFT method using the same basis set. In the next step, the electronic structure of the model compounds was evaluated in terms of Mulliken population analysis (MPA) such as spin densities (more exactly, the differences between α and β electron populations) on individual atoms using the 6-311G basis set for all atoms (basis II). All of the basis sets used are included in the Gaussian 03 library.[30]

RESULTS AND DISCUSSION

Template condensation of 3,5-di-*tert*-butyl-2-hydroxybenzaldehyde S-methylisothiosemicarbazone with pentane-2,4-dione and triethyl orthoformate at 105 °C afforded metal complexes of the type $M^{II}L$, where M = Ni and Cu, and H_2L is a novel tetradentate ligand (Scheme 1). Evidence for the formation of NiL and CuL was furnished by the positive ion ESI mass spectra, which showed the presence of peaks with m/z 510 attributed to $[NiL + H]^+$ and 493 and 515 assigned to $[CuL + H]^+$ and $[CuL + Na]^+$, respectively. Related complexes of copper(II) and nickel(II) with tetradentate ligands unsubstituted in positions 3 and 5 of the phenol ring (Chart 3, R = S-alkyl) were obtained analogously and reported previously.[31−34] Heating pentane-2,4-dione with triethyl orthoformate affords 3-ethoxymethylene-pentane-2,4-dione (the latter hydrolyzes with formation of 3-formyl-pentane-2,4-dione), which then undergoes a condensation reaction with the terminal NH_2 group of the tridentate thiosemicarbazone. Attempts to perform this reaction in the absence of metal as a template failed. It should, however, be noted that the synthesis of metal-free tetradentate Schiff base H_2L^1 (R = SCH_3) was realized in the presence of VO^{2+} and Zn^{2+}, making use of their catalytic coordination template effect.[31,35] Demetalation of $Ni^{II}L$ with gaseous hydrogen chloride in chloroform afforded the metal-free ligand H_2L. The latter showed in the mass spectrum peaks at m/z 432 and 454, which correspond to $[H_2L + H]^+$ and $[H_2L + Na]^+$, respectively. By reaction of the latter with $Zn(CH_3COO)_2 \cdot 2H_2O$ in a 1:1 molar ratio in 1:2 chloroform/methanol, the complex $ZnL(CH_3OH)$ was isolated. The ESI mass spectrum contains two peaks at m/z 494 and 516, which can be attributed to $[ZnL + H]^+$ and $[ZnL + Na]^+$, correspondingly.

The results of X-ray diffraction studies of NiL, CuL, $ZnL(CH_3OH)$, H_2L, and CuL^{Me} are shown in Figures 1−4, correspondingly. Selected bond distances (Å) and angles (deg) are quoted in Table 2. The metal ion is coordinated by two nitrogens (N1, N3) and two oxygen atoms (O1, O2). In ZnL, the apical coordination site is occupied by a molecule of methanol. The coordination geometry about nickel(II) and copper(II) can be described as square-planar. The coordinated atoms O1, O2, N1, and N3 are almost coplanar with deviations from the mean planes within ±0.004 and ±0.001 Å for two independent molecules in NiL, and strictly coplanar in CuL. The dihedral angle between the two O−Ni−N planes in two crystallographically independent molecules of NiL is at 178.8 and 178.4°, while in CuL is at 180°. The coordination polyhedron of zinc(II) in $ZnL(CH_3OH)$ is a square-pyramid (τ = 0.02).[36] The coordinated atoms O1, O2, N1, and N3 in the basal plane of the pyramid in $ZnL(CH_3OH)$ deviate from the least-squares plane defined by N_2O_2 atoms within ±0.029 Å. The zinc ion comes out from this plane by 0.401 Å toward the apical ligand. The configurations adopted by the ligand in metal complexes and in the metal-free state are quite different. The ligand is in *Z* configuration with respect to the central N2═C8 bond in NiL, CuL, and $ZnL(CH_3OH)$, while in the *E* configuration in H_2L. For metal coordination, two rotations of the relevant moiety in the metal-free ligand are required, one around the N2═C8 bond and the second around the N3−C8 bond. Note that the *E* configuration has been also established for H_2L^1 (R = S-*n*-C_3H_7)[31,34] by X-ray diffraction (Chart 3). In this last structure, however, the phenolic proton was not involved in an intramolecular hydrogen bonding to the azomethine nitrogen atom.

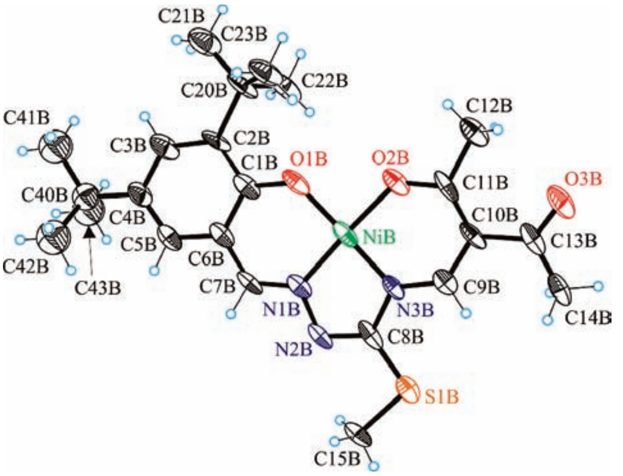

Figure 1. ORTEP view of the second crystallographically independent molecule of NiL in the asymmetric unit with atom labeling and thermal ellipsoids at the 50% probability level.

The doubly deprotonated tetradentate ligand L^{2-} forms three metallocycles on coordination to the metal, one five-membered A and two six-membered B and C (see Scheme 1). The Ni−O1, Ni−O2, Ni−N1, and Ni−N3 distances in two crystallographically independent molecules A and B (Table 2) are comparable to analogous parameters in NiL^1 (R = SCH_3) at 1.843(3), 1.847(3), 1.829(4), and 1.843(3) Å.[33] The Cu−O1, Cu−O2, Cu−N1, and Cu−N3 distances in CuL (Table 2) are very similar to those in CuL^1 (R = S-*n*-C_3H_7)[34] at 1.879(3), 1.934(3), 1.914(3), and 1.921(2) Å, correspondingly.

Geometrical similarity is also observed for Zn−O1, Zn−O2, Zn−N1, and Zn−N3 distances in $ZnL(CH_3OH)$ (Table 2) and ZnL^1(pyridine) (R = S-*n*-C_3H_7)[35] at 1.942(5), 2.049(5), 2.079(6), and 2.089(5) Å, respectively.

Of note is the sequence of single and double bonds in the fragment C6−C7−N1−N2−C8−N3 with deviations from standard bond lengths, which is determined by π-delocalization. Strong π-delocalization is also evident in the pentane-2,4-dione moiety (Table 2).

The *E* configuration adopted by both crystallographically independent molecules of H_2L is not strictly planar. The dihedral angle between the mean plane through the isothiosemicarbazide moiety and benzene ring is 4.8 and 8.1°, while that between the

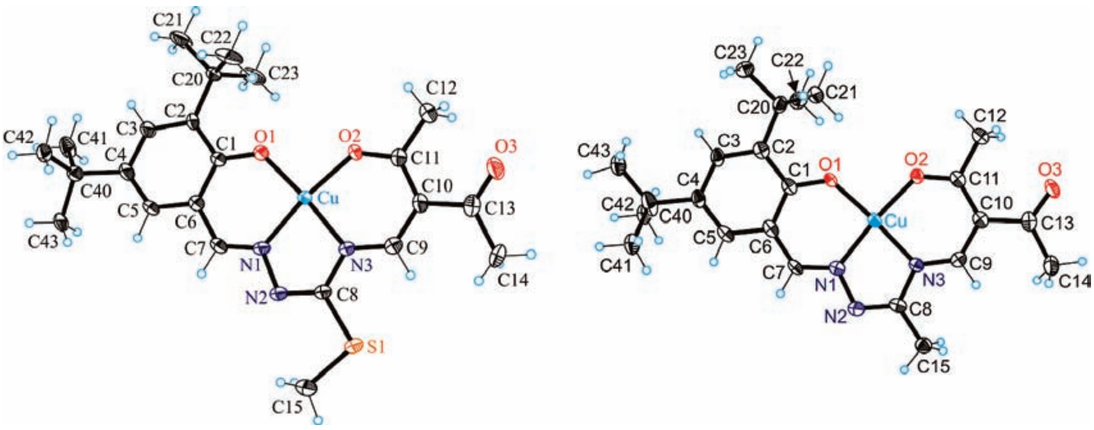

Figure 2. ORTEP view of the molecule of CuL (left) and CuL^{Me} (right) with atom labeling and thermal ellipsoids at the 50% probability level.

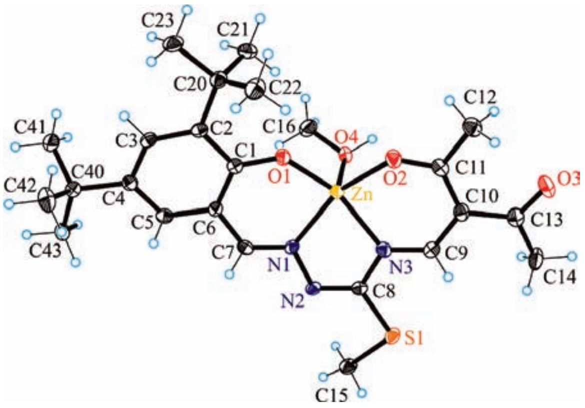

Figure 3. ORTEP view of the molecule of $ZnL(CH_3OH)$ with atom labeling and thermal ellipsoids at the 50% probability level.

same fragment and flat acetyl groups involved and not involved in intramolecular hydrogen bonding are at 19.1 and 24.1 and at 2.3 and 26.0° in molecules A and B, correspondingly. These dihedral angles are markedly different from the corresponding ones found in H_2L^1 ($R = SCH_3$) at 7.4, 7.0, and 10.2° due to the presence of bulky *tert*-butyl groups in H_2L and their effect on packing.

EPR Spectra for $Cu^{II}L$ and $Cu^{II}L^{Me}$. Figure 5 shows the EPR spectra of $Cu^{II}L$ in a mixture of CH_2Cl_2/DMF recorded at both X-band (~9 GHz, at 80 K) and Q-band (35 GHz, at 2 K) microwave frequencies. The essentially axial spectra were successfully simulated with $g_{||} \sim 2.226$ and $g_{\perp} \sim 2.055$ and ^{63}Cu hyperfine coupling constant $A_{||} \sim 640$ MHz. The two frequencies yielded slightly different sets of simulation parameters, so consensus values are given here; the Figure 5 caption gives the exact values. Besides experimental variability, the chief basis for the difference is due to the relative ability of X-band (and lower frequencies) to determine the field-independent hyperfine coupling and Q-band (and higher frequencies) to determine the field-dependent g values. These effects in the context of Cu(II) complexes have been discussed in detail by Hyde and Froncisz.[37] These spin Hamiltonian parameters are similar to those reported for other copper(II) complexes with a N_2O_2 coordination environment, for which $g_{||}$ is in the range of 2.20−2.25 and $A_{||}$ is in the range of 600−660 MHz, as compiled by Peisach and Blumberg.[38] The complex $Cu^{II}L$ thus shows no evidence by EPR of any effect of the phenolate ligand. As shown below, however, oxidation will lead to "non-innocent" ligand behavior.

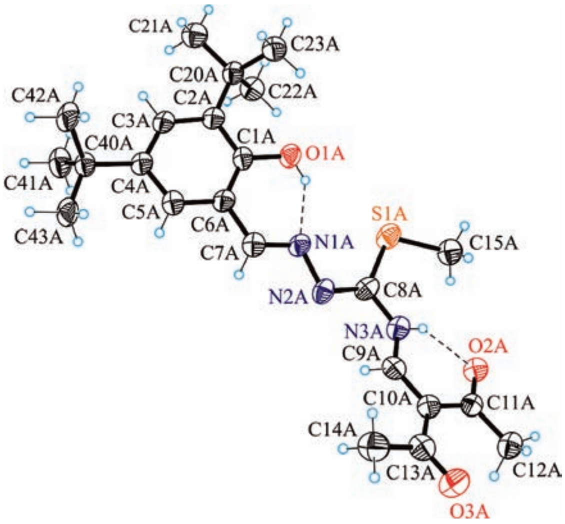

Figure 4. ORTEP view of one crystallographically independent molecule of H_2L with atom labeling and thermal ellipsoids at 50% probability level. Two intramolecular hydrogen bonds O1A−H···N1A [O1A−H, 0.84; H···N1A, 1.873; O1A···N1A, 2.606 Å; O1A−H···N1A, 144.94°] and N3A−H···O2A [N3A−H, 0.88; H···O2A, 1.878; N3A····O2A, 2.560 Å; N3A−H···O2A, 132.98°] are also shown.

The EPR parameters for $Cu^{II}L^{Me}$ determined from spectra recorded at both X- and Q-band frequencies (see Figure S1, Supporting Information) are essentially the same as those for $Cu^{II}L$.

Spectroelectrochemistry. Figure 6 shows cyclic voltammograms of the ligand H_2L and complexes $Ni^{II}L$, $Cu^{II}L$, and $Zn^{II}L \cdot CH_3OH$, at a scan rate of 0.10 V s^{-1} on a platinum wire working electrode. All potentials are referenced vs ferrocene/ferrocenium (Fc/Fc^+) as an internal reference redox couple. For H_2L, an irreversible one-electron oxidation wave with the highest oxidation potential at $E_p = 0.88$ V vs Fc/Fc^+ was observed, indicating a low stability of the emerging cation radical (phenoxyl radical) formed upon oxidation.

The formation of the phenoxyl radical was confirmed by an *in situ* EPR spectroelectrochemical experiment performed for H_2L in $TBAPF_6/CH_2Cl_2$ by using a large platinum mesh working electrode. A low intensity EPR signal with hyperfine splitting was observed in the region of the first electron transfer (Figure 7). The EPR signal of this species exhibits a lifetime of

Table 2. Selected Bond Lengths (Å) and Angles (deg)

	NiL				H_2L		
	Mol A	Mol B	CuL	$ZnL(CH_3OH)$	Mol A	Mol B	CuL^{Me}
M1−O1	1.8286(19)	1.829(2)	1.878(3)	1.926(2)			1.871(3)
M1−O2	1.8578(19)	1.8650(19)	1.933(2)	2.005(2)			1.918(3)
M1−N1	1.822(2)	1.821(2)	1.910(3)	2.036(2)			1.905(4)
M1−N3	1.811(3)	1.828(2)	1.925(3)	2.064(2)			1.914(4)
M1−O4				2.081(2)			1.925(3)
O1−C1	1.315(3)	1.308(3)	1.297(4)	1.309(3)	1.365(4)	1.369(4)	1.322(6)
C1−C6	1.418(3)	1.427(3)	1.437(5)	1.431(4)	1.402(5)	1.405(4)	1.434(7)
C6−C7	1.403(4)	1.428(4)	1.425(5)	1.441(4)	1.450(4)	1.466(4)	1.427(7)
N1−C7	1.309(4)	1.292(3)	1.295(5)	1.299(4)	1.289(4)	1.291(4)	1.309(6)
N1−N2	1.398(3)	1.405(3)	1.404(4)	1.399(3)	1.408(3)	1.415(3)	1.406(6)
N2−C8	1.305(4)	1.304(4)	1.289(5)	1.304(4)	1.292(4)	1.290(4)	1.306(6)
N3−C8	1.417(3)	1.394(3)	1.400(4)	1.401(4)	1.385(4)	1.383(4)	1.399(6)
N3−C9	1.341(3)	1.330(3)	1.327(5)	1.319(4)	1.343(4)	1.353(4)	1.326(6)
C10−C9	1.428(4)	1.391(4)	1.387(5)	1.410(4)	1.373(4)	1.371(4)	1.410(7)
C10−C11	1.411(4)	1.410(5)	1.446(5)	1.456(4)	1.484(5)	1.469(5)	1.439(7)
O2−C11	1.262(3)	1.275(3)	1.258(4)	1.259(4)	1.249(4)	1.245(4)	1.273(6)
O3−C13	1.225(3)	1.219(3)	1.228(6)	1.232(4)	1.230(4)	1.227(4)	1.225(6)
S1−C8	1.730(3)	1.739(3)	1.755(3)	1.760(3)	1.754(4)	1.764(3)	
O1−M1−N1	95.0(1)	95.0(1)	93.8(1)	90.13(9)			94.11(16)
O1−M1−N3	178.37(9)	178.02(9)	175.2(1)	153.68(10)			175.63(15)
N1−M1−N3	83.5(1)	83.4(1)	81.5(1)	77.07(9)			81.60(17)
O1−M1−O2	87.90(8)	87.78(9)	94.2(1)	97.77(8)			92.09(14)
N1−M1−O2	176.9(1)	177.0(1)	172.2(1)	155.09(9)			173.43(16)
N3−M1−O2	93.6(1)	93.8(1)	90.6(1)	85.81(9)			92.23(15)

only a few seconds (half-life time about 1 s in CH_2Cl_2), but a g value of 2.002 can be determined, which is typical for organic π-conjugated systems. By signal averaging, we were able to obtain sufficient signal-to-noise ratio to simulate this spectrum using the SimFonia (Bruker) program with the following hyperfine splitting constants: a_H 6.0, a_N 3.7, a_N 3.5, and a_H 0.4 G. This indicates delocalized spin density mostly over the substituted phenol ring and the neighboring π-conjugated −C═N−N═C− fragment. Additional evidence is provided by the composition of the α-HOMO orbital as well as from the calculated spin density distribution for $[H_2L]^{+\bullet}$ as depicted in Figure 8.

On going from the metal-free ligand H_2L to the corresponding metal complexes, a strong shift of oxidation potential was observed ($E_{1/2} = 0.38$ V for $Zn^{II}L(CH_3OH)$, $E_{1/2} = 0.62$ V for $Cu^{II}L$, and $E_{1/2} = 0.67$ V for $Ni^{II}L$). In addition, the oxidation peak becomes more reversible, especially for the $Cu^{II}L$ complex (Figure 6). At a scan rate of 0.10 V s^{-1}, we observed electrochemical reversibility for $Cu^{II}L$ similar to the ferrocene internal standard (Figure S2, Supporting Information). This indicates a marked stabilization of a phenoxyl radical within the complex formed upon the first electron transfer and a substantial contribution of metal orbitals. To elucidate the effect (if any) of the MeS group on the physicochemical properties of the complex, we prepared a new Cu(II) complex, CuL^{Me}, in which the MeS group was replaced by a Me group. The complex was studied by X-ray diffraction, EPR spectroscopy, and cyclic voltammetry. The replacement of MeS by Me has no effect on EPR parameters and redox potential nor on the reversibility of the one-electron oxidation voltammetric peak. Reversible electrochemical behavior and only a slight anodic shift of 10 mV compared to $Cu^{II}L$ were found for $Cu^{II}L^{Me}$. In contrast, an irreversible oxidation was observed for corresponding complexes without *tert*-butyl groups in both $Cu^{II}L^1$ and $Cu^{II}L^{1,Me}$ with a strong electrochemical potential shift of 110 mV (Figure S2, Supporting Information), confirming the important role of *tert*-butyl groups for both oxidation potential and the stabilization of the phenoxyl radical within the complex.

As no change in the redox state of zinc(II) in $Zn^{II}L(CH_3OH)$ was expected for its one-electron oxidation, we first studied its oxidation by *in situ* spectroelectrochemistry. Figure 9 shows an evolution of UV−vis−NIR spectra monitored upon anodic oxidation of $Zn^{II}L(CH_3OH)$ in $TBAPF_6/CH_2Cl_2$ in the region of the first electron transfer. It can be seen that two new absorption bands emerge at 550 and 1125 nm. Such bands are characteristic of delocalized cation radicals as already well-documented for a variety of π-conjugated organic compounds (these are mostly attributed to the HOMO−SOMO and SOMO−LUMO transitions).[39,40]

The EPR activity of the formed species was proved by *in situ* EPR spectroelectrochemistry. A narrow EPR line without hyperfine splitting and g value of 2.0027 was registered for the one-electron oxidized $[ZnL(CH_3OH)]^+$, indicating delocalized spin and ligand centered character of this EPR signal (Figure S3, Supporting Information). It should be noted that a similar sharp EPR line was observed upon oxidation of $Ni^{II}L$, but the g value is shifted to $g = 2.0137$. This signal can be assigned to a species of predominantly phenoxyl radical character with marked contribution from the central atom ($g > 2.00$ results from the contribution of Ni^{II} with its more than half-filled ($3d^8$) configuration).[16] As seen for $ZnL(CH_3OH)$ oxidation, UV−vis−NIR spectra

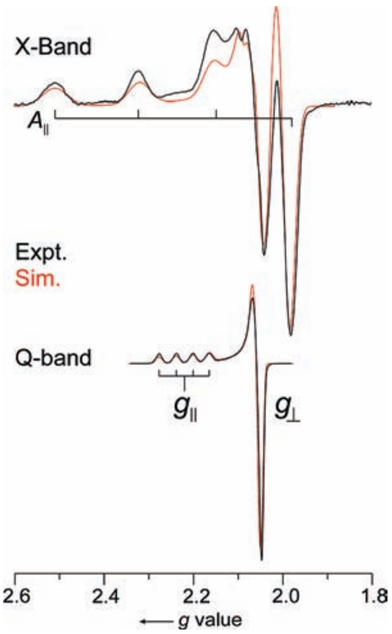

Figure 5. X-band (upper) and Q-band (lower) EPR spectra of $Cu^{II}L$ in 1:1 v/v CH_2Cl_2/DMF. The spectra are displayed on a descending g value scale to allow comparison between the two frequencies. Experimental parameters, X-band: temperature, 80 K; microwave frequency, 9.215 GHz; 100 kHz field modulation amplitude, 5 G; time constant, 30 ms; scan time, 2 min. Q-band: temperature, 2 K; microwave frequency, 35.102 GHz; 100 kHz field modulation amplitude, 0.16 G; time constant, 4 ms; scan time, 4 min. Simulation parameters, X-band: $\mathbf{g}$ = [2.05, 2.06, 2.235], $\mathbf{A}(^{63}Cu)$ = [60, 60, 670] MHz; $A_{iso}(^{14}N)$*2 = 40 MHz; single crystal Gaussian linewidths (hwhm), $W_{\perp}$ = 30 MHz, $W_{||}$ = 90 MHz. Q-band: $\mathbf{g}$ = [2.05, 2.06, 2.218], $\mathbf{A}(^{63}Cu)$ = [60, 60, 600] MHz; $A_{iso}(^{14}N)$*2 = 40 MHz; single crystal Gaussian linewidths, $W_{\perp}$ = 50 MHz, $W_{||}$ = 140 MHz.

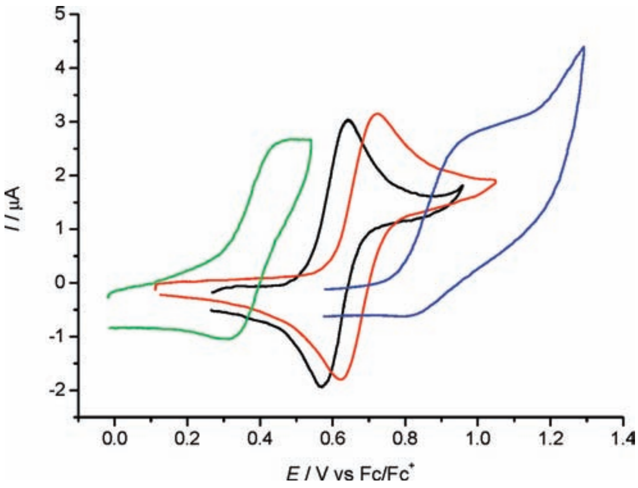

Figure 6. Cyclic voltammograms of H_2L (blue line), $Zn^{II}L \cdot CH_3OH$ (green line), $Cu^{II}L$ (black line), and $Ni^{II}L$ (red line) in 0.20 M $TBAPF_6$/CH_2Cl_2 solutions at a scan rate of 0.10 V s^{-1}.

monitored upon anodic oxidation of $Ni^{II}L$ as well as $Cu^{II}L$ in $TBAPF_6$/CH_2Cl_2 in the region of the first electron transfer exhibit at room temperature new absorption bands at 595, 827, and 1092 nm for $[NiL]^+$ and at 540 and 1175 nm for $[CuL]^+$ (Figure 10), indicating ligand centered spin delocalization by analogy with the results for $Zn^{II}L$. The lifetime of these products was determined to be several tens of seconds (half-life $t_{1/2}$ = 38 s for CuL^+), indicating essential stabilization of the phenoxyl radical within the metal complex compared to the metal-free ligand.

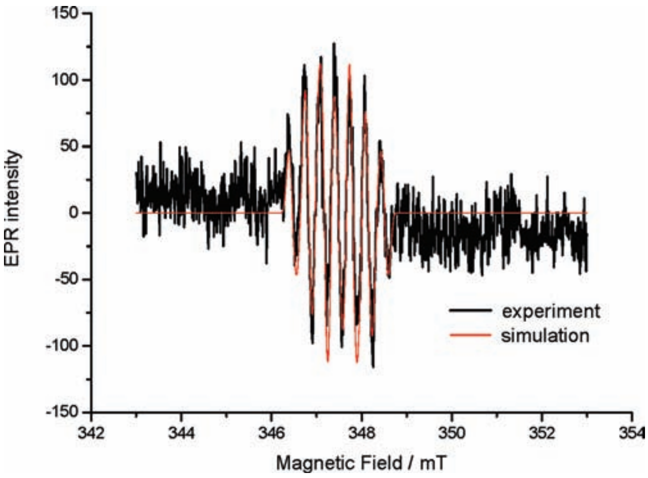

Figure 7. EPR spectrum observed upon oxidation of H_2L in $TBAPF_6$/CH_2Cl_2. Experimental EPR parameters, X-band: temperature, 298 K; microwave frequency, 9.795 GHz; microwave power, 10 mW; modulation amplitude, 2G; time constant, 41 ms; scan time, 84 s.

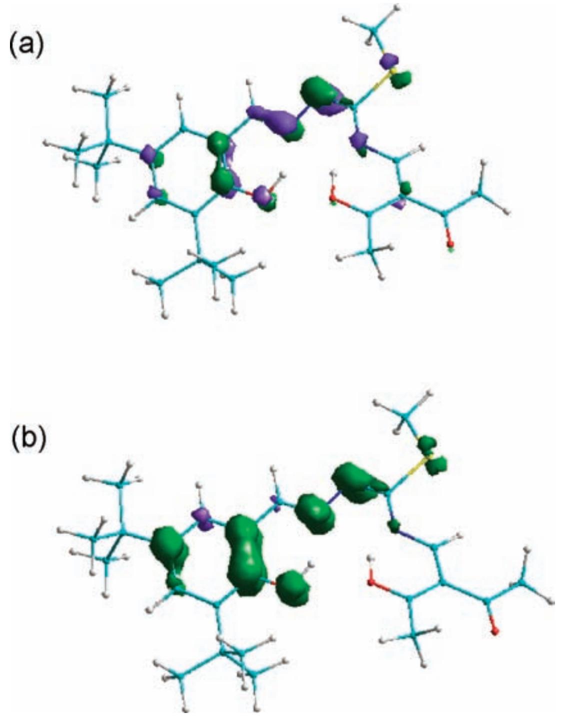

Figure 8. (a) α-HOMO (0.07 isosurface level) orbital and (b) spin density (0.005 isosurface level) of $[H_2L]^+$.

Computed HOMO orbitals of $Ni^{II}L$ and $Zn^{II}L$ complexes as well as the α-HOMO of $Cu^{II}L$ indicate the same dominating redox site for oxidation as observed for H_2L, with additional contributions from the Ni and Cu d-orbitals (see below). Frontier MOs of $Ni^{II}L$ are of π character with α and β ones being very similar. The HOMO is located mainly on the benzene ring and its phenolate oxygen and on the hydrazine residue

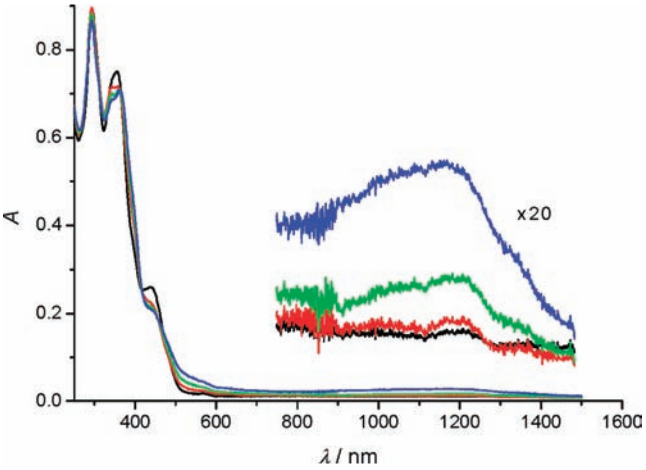

Figure 9. UV−vis−NIR spectroelectrochemistry of $Zn^{II}L(CH_3OH)$ in $TBAPF_6/CH_2Cl_2$ recorded in the region of the first electron transfer using a Pt mesh working electrode (black line, 0.0 V; red line, 0.3 V; green line, 0.4 V; blue line, 0.5 V vs Fc/Fc^+). The inset shows an expansion (20×) of the NIR bands.

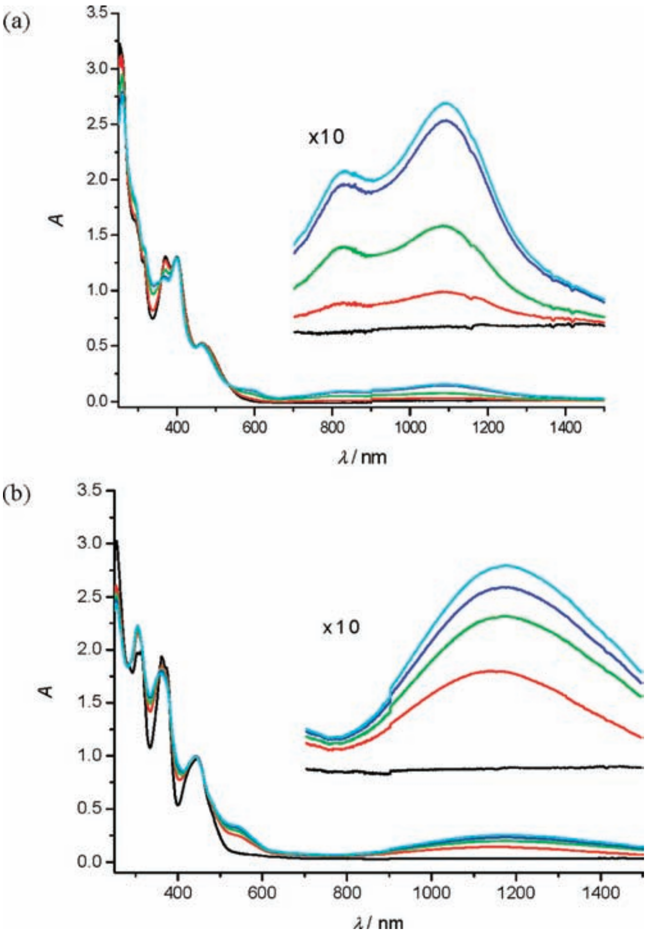

Figure 10. UV−vis−NIR spectroelectrochemistry of (a) $Ni^{II}L$ (black line, 0.5 V; red line, 0.6 V; green line, 0.7 V; blue line, 0.8 V; cyan line, 0.9 V vs Fc/Fc^+) and (b) $Cu^{II}L$ (black line, 0.50 V; red line, 0.55 V; green line, 0.60 V; blue line, 0.65 V; cyan line, 0.70 V vs Fc/Fc^+) in $TBAPF_6/CH_2Cl_2$ using a Pt mesh working electrode in the region of the first electron transfer. The insets show expansions (10×) of the NIR bands.

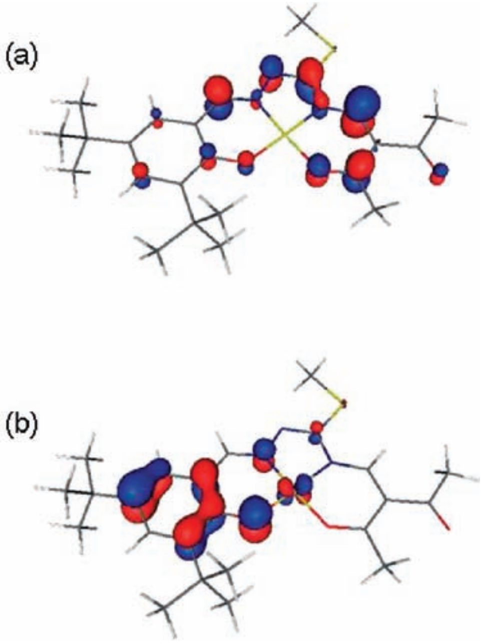

Figure 11. LUMO (a) and HOMO (b) for $Ni^{II}L$ [E(LUMO) = −0.0851 and E(HOMO) = −0.1955 au].

nitrogen atom bound to the nickel(II) with a moderate antibonding contribution of out-of-plane d(Ni) orbitals (Figure 11b). The LUMO is localized mainly on the ligand framework accommodating the metal without any Ni contribution (Figure 11a). The β-LUMO of $[NiL]^+$ is very similar to the HOMO of NiL, but its α counterpart exhibits an analogy to the LUMO of NiL (Figure S4c and a, Supporting Information). The practically equal in-plane α and β HOMOs of $[NiL]^+$ (Figure S4b and d, Supporting Information) are of σ character and are located on the noncoordinated acetyl group.

All frontier MOs of $Cu^{II}L$ are of π character, with α and β ones being very similar (Figure S5, Supporting Information). Both HOMOs are very similar to those of $Ni^{II}L$, but with a smaller antibonding contribution of out-of-plane d(Cu) orbitals. The LUMOs are also analogous to those of $Ni^{II}L$ without any Cu contribution. The HOMO of $[CuL]^+$ resembles those of $Cu^{II}L$, but the corresponding LUMO is of σ character and located on in-plane d(Cu) orbitals and adjacent donor atoms with antibonding d−p interactions (Figure S6, Supporting Information).

The frontier MOs of ZnL are of π-character and located mainly on the chelate rings without any Zn contribution, the HOMO having significant phenolate ring contributions (Figure S7, Supporting Information). The α-LUMO of $[ZnL]^+$ looks analogous to the LUMOs of CuL, whereas its β-LUMO counterpart exhibits a close analogy to the HOMOs of CuL, but without any Zn contribution (Figure S8, Supporting Information). The β-LUMO of $[ZnL]^+$ is very similar to the HOMO of ZnL, whereas the β-HOMO of $[ZnL]^+$ is of σ character and located prevailingly on noncoordinated acetyl group as in HOMOs of $[NiL]^+$.

The spin density distribution in the $[NiL]^+$, $[Cu^{II}L]$, and $[ZnL]^+$ complexes differs significantly from the corresponding α-HOMO shapes (Figure 12). For all three metal complexes, it has out-of-plane π-character and is located on carbon atoms of the aromatic ring and the phenolic oxygen and hydrazine residue nitrogen atoms bound to the metal atom. Unlike $[Cu^{II}L]$ and

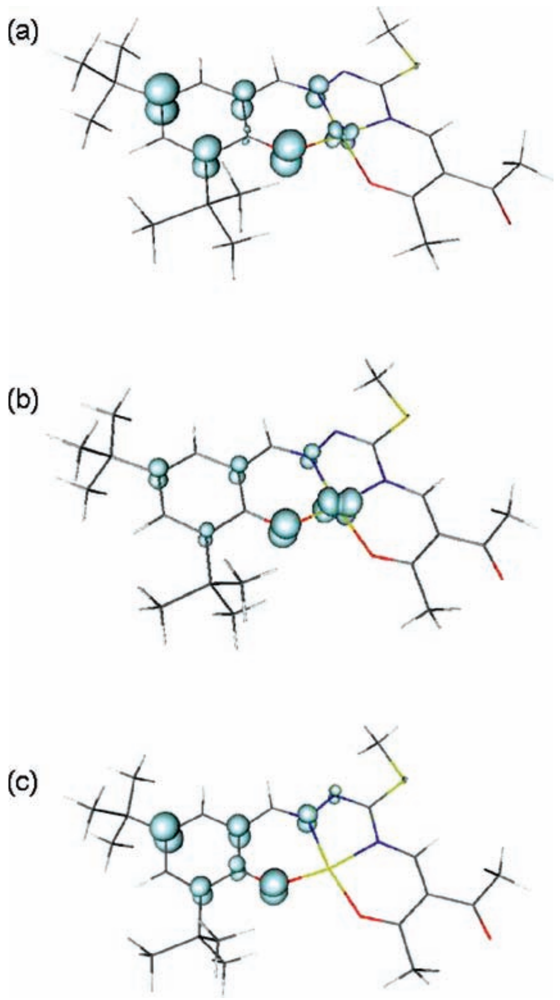

Figure 12. Spin density distribution in $[NiL]^+$ (a), [CuL] (b), and $[ZnL]^+$ (c) complexes.

$[NiL]^+$ complexes, the $[ZnL]^+$ system carries no spin density on the metal atom, and this is shifted onto the hydrazine residue.

In the case of $Cu^{II}L$ oxidation in $TBAPF_6/CH_2Cl_2$ at room temperature directly in the optical EPR cavity (enabling simultaneous monitoring of UV−vis spectra), a new absorption band at 540 nm (2.25 eV) arises during oxidation upon the first electron transfer (Figure 13a) with a simultaneous decrease of the characteristic EPR signal of the $Cu^{II}L$ complex (Figure 13b). Unlike for $Zn^{II}L(CH_3OH)$ and $Ni^{II}L$ oxidation, there was no new EPR sharp line emerging.

Taking into account the results from EPR/UV−vis spectroelectrochemistry of $Cu^{II}L$ shown above, it can be concluded that the quenching of the EPR signal during the oxidation could be due to an antiferromagnetic spin-coupling between the unpaired electron on Cu^{II} and the unpaired electron on the ligand, as already reported both for copper(II) salen monomers and in the case of a copolymer containing copper(II) salen and 3,4-ethylenedioxythiophene units.[41,42] This indicates that the divalent state of Cu is still dominating in the one-electron oxidized $[CuL]^+$ complex at room temperature, similar to $[NiL]^+$ and $[ZnL]^+$. It should be noted that although a not-fully reversible CV wave has been observed at very slow scan rates (3 mV s^{-1}), almost chemically reversible redox behavior was observed for $Cu^{II}L$ oxidation in the region of the first electron transfer. The electronic absorption spectra measured upon direct and reverse voltammetric scans are very similar (Figure S9, Supporting Information).

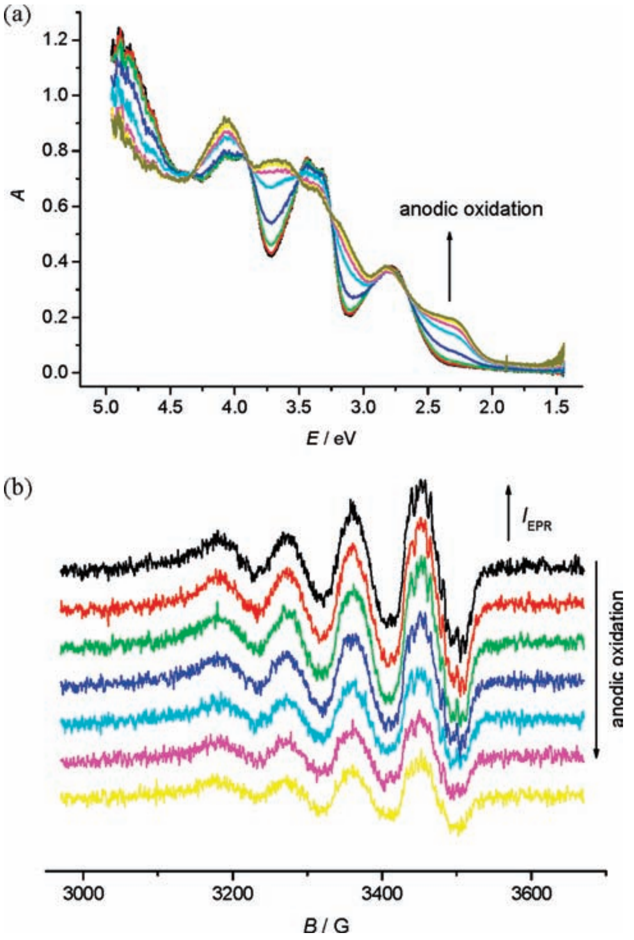

Figure 13. *In situ* ESR−UV−vis spectroelectrochemistry of $Cu^{II}L$ in $TBAPF_6/CH_2Cl_2$ using a large platinum working electrode. UV−vis (a) and EPR (b) spectra measured during oxidation (UV−vis and EPR traces recorded at the same time point of measurement have the same color; EPR spectra are shifted on the Y-scale for clarity).

Although some evidence has been provided for a dominating M(II)−phenoxyl radical state at room temperature for the investigated complexes, there are several examples in the literature confirming the presence of both $[M^{II}(L^{-\bullet})]^+$ and $[M^{III}(L^{2-})]^+$ states, particularly for oxidized nickel(II) complexes. Temperature-dependent tautomerism between nickel(III)−phenolate and nickel(II)−phenoxyl radical states was observed.[16,18] To investigate this possibility for our oxidized $[NiL]^+$, we performed an *ex situ* spectroelectrochemical experiment. The $Ni^{II}L$ sample was electrolyzed in $TBAPF_6/CH_2Cl_2$ directly in an X-band EPR tube using a platinum mesh working electrode. This EPR tube was then immediately immersed into liquid nitrogen, and EPR spectra were recorded at 77 K. Figure 14 shows the EPR spectrum of the one-electron oxidized $[NiL]^+$ complex measured in this way. It exhibits two anisotropic EPR spectra with different *g* values, in contrast to the single isotropic EPR signal ($S = 1/2$) measured at room temperature. At room temperature, the *g* value of 2.014 is between that for the oxidized $[ZnL]^+$ complex and typical Ni(III) complexes (see below), indicating the formation of a ligand radical with partial

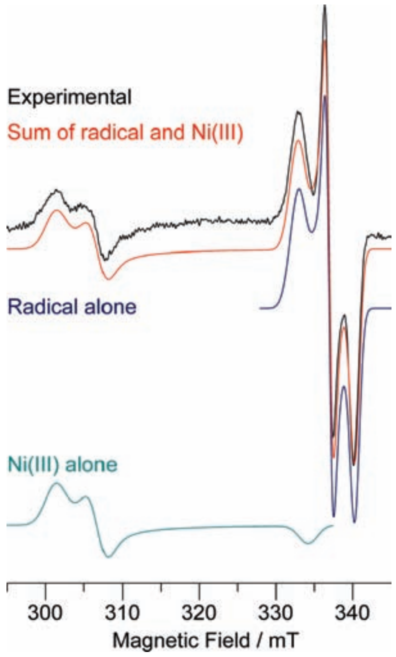

Figure 14. X-band EPR spectrum of oxidized $Ni^{II}L$ with simulations as described in the text. Experimental EPR parameters, X-band: temperature, 77 K; microwave frequency, 9.497 GHz; microwave power, 10 mW; modulation amplitude, 5G; time constant, 82 ms; scan time, 42 s.

delocalization of the unpaired spin onto orbitals of the nickel ion.[18] At 77 K, this "radical" signal still dominates the EPR spectrum due to its narrowness but becomes anisotropic with a rhombic pattern. Simulation of this signal[43] yields $\mathbf{g} = [2.039(1), 2.014(1), 1.994(1)]$. The linewidths are also anisotropic ($W = 35, 15, 20$ MHz; Gaussian, hwhh), which may be due to unresolved ^{14}N and/or ^{1}H hyperfine coupling. The data did not warrant any attempt to extract hyperfine coupling parameters. The new "metal" EPR signal, which we attribute to a Ni(III) species (see below), is broader and as a result gives the appearance of being less significant. In this case, it is possible to determine definitively only the perpendicular region parameters, as the parallel feature is likely masked by the radical signal. However, the comparison of the simulated and experimental radical spectra suggests an estimate as to the g_{min} ($g_{\parallel}$) value for this Ni(III) species. The simulated spectrum at 335 mT has higher intensity than the experimental spectrum, yet matches perfectly elsewhere. We propose that this is due to the contribution of the downward $g_{\parallel}$ feature of the Ni(III) species. This is shown in Figure 14, which displays the sum of the simulations as well as the simulation of the Ni(III) and radical species alone. With this assumption, the Ni(III) species gives $\mathbf{g} = [2.252(1), 2.212(1), 2.03(1)]$ with $W = 50, 40$, and 40 MHz (Gaussian, hwhh). Scaling of the simulated intensities to match experimental results at g_{mid} of each, followed by double integration, indicates that the Ni(III)−phenolate species is slightly more prevalent than the Ni(II)−phenoxyl radical species (1.04:1.00). The $\mathbf{g}$ matrix deduced for the Ni(III) species is characteristic of the low-spin $3d^7$ electronic configuration with a $(d_{xy,yz,xz})^6 d_{z^2}{}^1$, ground state, such as often found for Co(II).[44] This result is also the case for complexes that, due to their having fully saturated azamacrocyclic ("innocent") ligands, unequivocally contain Ni(III).[45] Examples of authentic Ni(III) include complexes such as $[Ni(tacn)_2]^{3+}$ (tacn = 1,4,7-triazacyclononane), for which $g_{\perp} = 2.128$ and $g_{\parallel} = 2.026$ as a powder at 150 K,[46] and $[Ni(Me_2[14]aneN4)Cl_2]^+$,[47] for which $g_{\perp} = 2.181$ and $g_{\parallel} = 2.025$ as a powder at ~300 K. The Ni(III) form of the partly unsaturated tetraazamacrocyclic F430 cofactor isolated from methyl Coenzyme M reductase (MCR) likewise has $g_{\perp} = 2.211$ and $g_{\parallel} = 2.020$.[48] The N_2O_2 donor set for $Ni^{III}L$ leads to the slightly rhombic EPR spectrum compared to the axial spectra of these complexes with N4 donors.[44]

Thus, the $Ni^{II}L$ oxidized by one electron exhibits temperature-dependent valence tautomerism between nickel(III)−phenolate species and its nickel(II)−phenoxyl radical counterpart. At room temperature, the $[Ni^{II}(L^{-\bullet})]^+$ is the only detectable complex, while at 77 K, both species, $[Ni^{II}(L^{-\bullet})]^+$ and $[Ni^{III}(L^{2-})]^+$, are present in a ~1:1 molar ratio.

Electronic Absorption Spectra. In Figure 15, experimental electronic absorption spectra for CuL, NiL, and ZnL are compared with theoretical electronic transitions calculated for both $M^{II}L$ (in black) and oxidized $[ML]^+$ (in red) species, while the experimental absorption spectrum of H_2L is given for comparison in Figure S10 (Supporting Information). On the basis of the optimal geometries, the electronic transitions and related oscillator strengths were calculated using TD-DFT method. The first transition with relevant oscillator strength corresponds to that from HOMOs to LUMOs (H to L) for all $M^{II}L$ complexes. We recall that the α-HOMO (i.e., SOMO) of CuL and HOMO of NiL are of π character, located mainly on a benzene ring with a contribution from the central atom (see MOs in Figures S5 and 11, Supporting Information). On the other hand, the corresponding LUMOs are located mainly on the ligand framework accommodating the metal without any central atom contribution. Consequently, this transition can be attributed to charge transfer from the benzene ring and metal orbitals to the remaining part of the tetradentate ligand. For the ZnL complex, no metal contribution is seen in both frontier MOs, but a trace sulfur contribution to the HOMO was found (Figure S7, Supporting Information). Therefore, the HOMO to LUMO transition for ZnL takes place within the ligand with lower electron density transfer from the benzene ring to the remainder of the ligand than for Ni and Cu complexes. Other dominant TD-DFT-computed transitions correlate well with experimental spectra with a wide variety of MO combinations, as indicated in Figure 15.

For one-electron oxidized species, new transitions at lower energies which correspond well to the experimental data were obtained (see the experimental spectra in red and corresponding TD-DFT transitions in Figure 15). As the triplet state shows lower energy compared to the singlet one in vacuo (see the Supporting Information, Table S1), both triplet and singlet states were calculated for $[CuL]^+$ (Figure 16). The lowest energy electron transitions at 1 eV observed for the $[CuL]^+$ triplet can be attributed to the electron density transfer from the π-β-HOMO−1 localized mainly on the π-conjugated $-C{=}N-N{=}C-$ fragment to the π-β-LUMO located on the substituted phenolate ring (see MOs of the triplet state $[CuL]^+$ in Figure S11, Supporting Information).

On the other hand, the lowest energy electron transitions around 1 eV observed for the $[CuL]^+$ singlet state (see blue bars in Figure 16) can be attributed to the unusual electron density transfer from the π-HOMO localized mainly on the benzene ring to the σ-LUMO located at Cu and neighboring atoms (see MOs of $[CuL]^+$ singlet in Figure S6, Supporting Information).

For the $[NiL]^+$ complex, the lowest transition at 1.3 eV corresponds to the charge-transfer within the ligand from π-MO with a dominant sulfur contribution to the benzene ring part

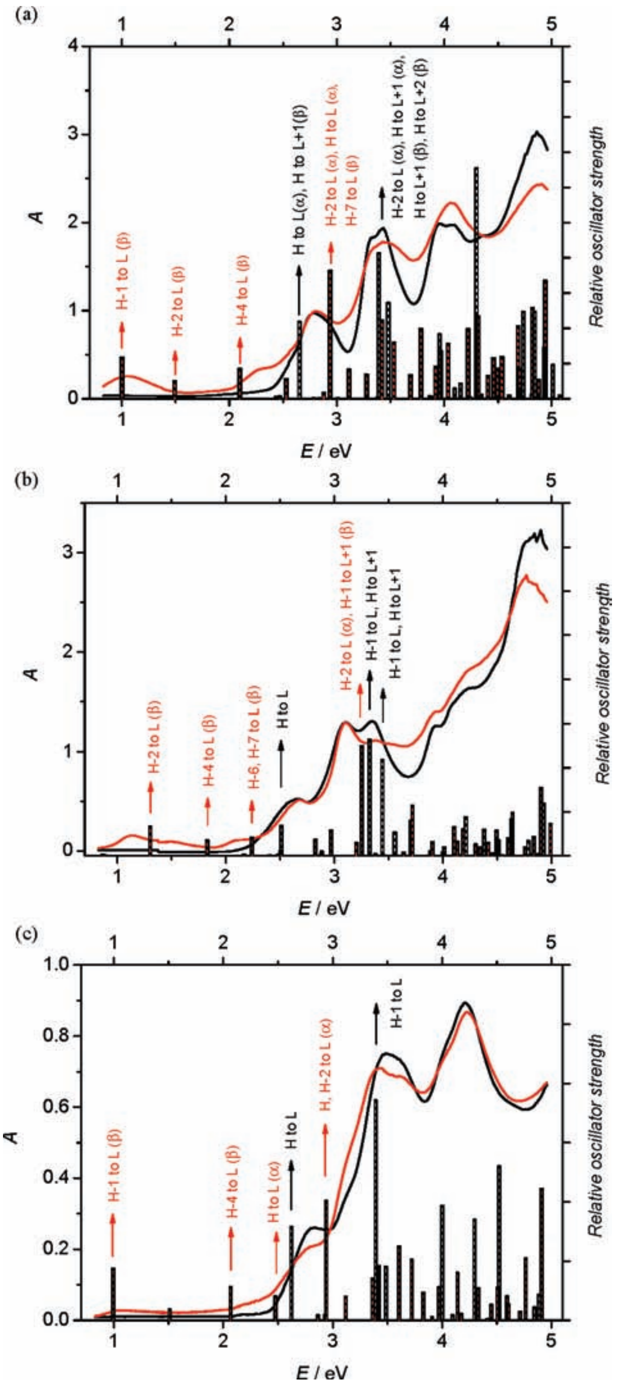

Figure 15. Comparison of the experimental electronic absorption spectra for CuL (a), NiL (b), and ZnL (c) with calculated electronic transitions both in neutral ($[ML]^0$, in black) and oxidized ($[ML]^+$, in red) states. Abbreviation for transition labels: H = HOMO, L = LUMO.

of the molecule. For the $[ZnL]^+$ complex, the electronic transition at 1 eV corresponds to the charge-transfer within the π-system of the ligand without any contribution from the central atom.

DFT CALCULATIONS

In the first step, the geometries of the H_2L ligand and ML complexes, M = Cu, Ni, and Zn, as well as of their monocations were optimized in the lowest spin states (Figure S12, Tables S2−S9, Supporting Information). The calculated spin densities on the $[H_2L]^{+\bullet}$ cation radical enabled us to select the most probable values of hyperfine splitting constants among various possible interpretations of experimental data by SimFonia program simulations.

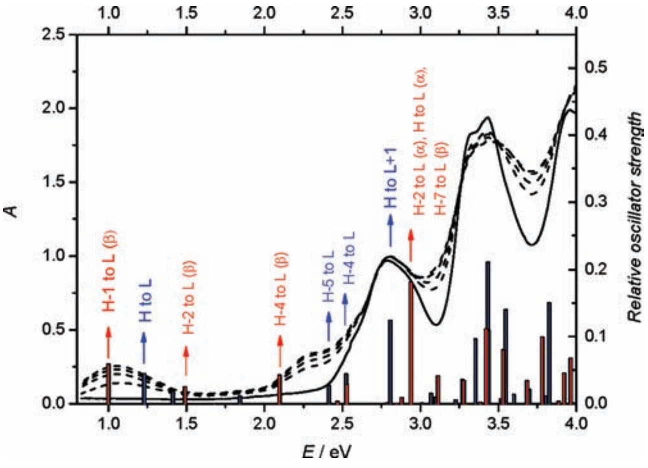

Figure 16. Comparison of the experimental electronic absorption spectra for CuL (black solid line) and $[CuL]^+$ (observed upon its oxidation at the first anodic peak, dashed black lines) with calculated electronic transitions for both $[CuL]^+$ in triplet (in red) and in singlet (in blue) states. Abbreviations for transition labels: H = HOMO, L = LUMO.

In the next step, the ML and $[ML]^+$ structures in higher spin states were optimized (Tables S10−S12, Supporting Information). We have found that the triplet $[CuL]^+$ structure is more stable (*in vacuo*) than the singlet by 0.4 eV (see Table S1, Supporting Information). If this is the case in solution as well, then such a spin triplet could in principle be observed by EPR, as is the case for many organic triplets and some inorganic species as well.[49] The inability to see EPR in our experiment might be due to the properties of the triplet being unsuitable for observation by conventional EPR (e.g., its zero-field splitting (*D* value) might be larger than the X-band microwave energy, ~0.3 cm^{-1}). On the other hand, the optimal quartet $[NiL]^+$ structure is less stable by 0.7 eV (see Table S1, Supporting Information) than the doublet state, whereas the neutral NiL complex prefers the lowest singlet state over the triplet by 1.8 eV. Our attempts to find a second stable structure of NiL^+ in a doublet electron state to explain its temperature-dependent redox tautomerism (see above) were not successful.

Using TD-DFT calculations, optical transitions in the complexes under study both in neutral and in monocharged states observed in spectroelectrochemistry have been successfully attributed to the concrete transitions with a description of the nature of these processes. Thus, ligand−ligand and metal−ligand transitions within the charged complexes have been identified. The shape and distribution of (α-)HOMO orbitals of the neutral complexes indicate clearly the redox site where the first oxidation event takes place.

FINAL REMARKS

By exploiting the template methodology, the synthesis of a new ligand with a N_2O_2 donor set which contains a single phenolic moiety, suitably protected by bulky *tert*-butyl substituents in the ortho and para positions of the parent phenol able to generate a phenoxyl radical, and which contains a thiomethyl group attached to the extended π-conjugated ligand framework has been realized. This ligand proved to be suitable for the synthesis of metal complexes as models for mimicking the electronic structure and/or functional properties of the active site in galactose oxidase (GAO) and glyoxal oxidase (GLO), as described below. One-electron electrochemical oxidation of the ligand (H_2L) gives rise to a cation radical $H_2L^{+\bullet}$, detectable at room temperature. The formation of the phenoxyl radical was confirmed by *in situ* EPR spectroelectrochemical data. The EPR signal with $g = 2.002$ is typical for a delocalized π-radical. Hyperfine splitting constants a_H 6.0, a_N 3.7, a_N 3.5, and a_H 0.4 G indicate delocalization over the substituted benzene ring and the adjacent π-conjugated $-C{=}N{-}N{=}C-$ fragment. Additional evidence is provided by the location of the HOMO of H_2L as well as from a calculated spin density distribution for $[H_2L]^{+\bullet}$. Further stabilization of phenoxyl radicals without any contribution from redox-inactive Zn^{2+} or with some contribution from d orbitals of redox-active metal ions (Ni^{2+}, Cu^{2+}) was observed in one-electron oxidized complexes $[ML]^+$ at room temperature. The square-planar complex $[CuL]^+$ does not contain a low-spin Cu(III) ion, but rather a Cu(II) ion ($3d^9$, $S_{Cu} = 1/2$), which is magnetically coupled to the ligand radical. Temperature dependent valence tautomerism in which the equilibrium shifts from a nickel(II)−phenoxyl toward a nickel(III)−phenolate complex has been also observed. X-band EPR spectra at 77 K indicate that the Ni(III) phenolate species is slightly more prevalent then the Ni(II)−phenoxyl species (1.04:1.00). We have communicated previously[50] on the effectiveness of nickel(II) and copper(II) complexes with related tetradentate ligands in the epoxidation of norbornene with molecular oxygen (1 atm) in THF at 70 °C. We will therefore further explore the catalytic ability of the metal phenolate and phenoxyl radical species reported herein on alcohol and other organic substrate oxidation reactions.

Our interest in model compounds with one phenolate unit was stimulated by the fact that copper(II) complexes with ligands which contain one phenolate moiety were reported[51,52] to show absorption bands in the visible and NIR regions of striking similarity to those of active GAO (λ_{max} = 444 nm and a broad structured band with a maximum at 800 nm) and GLO (448 and 851 nm) enzymes, and, therefore, are good systems for reproducing the spectroscopic features of these enzymes. Our compounds are able to generate one phenoxyl radical in a metal-free or metal coordinated state by electrochemical oxidation. The metal-free phenoxyl radical is not stable but can be detected by EPR spectroscopy. Its lifetime is only a few seconds. It is worth noting that we did not find metal-free phenoxyl radical species generated from salen-type ligands—the popularly used ligand for GAO/GLO model chemistry—in the literature. A marked stabilization of the phenoxyl radical is observed in metal complexes, as demonstrated by cyclic voltammetry, EPR spectroscopy, and UV−vis−NIR studies. The reversible character of the one-electron oxidation wave for CuL is clearly shown in Figure S2 (Supporting Information). The optical spectrum of $[CuL]^+$ shows two maxima at 540 and 1175 nm red-shifted compared to those characteristic for native enzymes. The structural modifications performed permitted to demonstrate that the thiomethyl group has no effect on redox potential and stabilization of the phenoxyl radical, as well as on EPR parameters. This is in contrast to the results reported by others[53] that a large cathodic shift in the oxidation potential was observed for the model compound with a thiomethyl group in the ortho position of the phenol ring as compared to an unsubstituted phenol derivative. This shift was attributed to both the electron-donating nature and the radical stabilizing effect by electron spin-delocalization into the thiomethyl group, referred to as an electron-sharing conjugative effect. Our experimental and DFT calculation data do not suggest electron spin-delocalization into the remote SCH_3 group. The effect of sulfur is secondary and confined to improved solubility in common organic solvents and increased thermal stability. In contrast, the effect of *tert*-butyl groups on stabilization of the phenoxyl radical and on the reversibility of one-electron oxidation is evident. Only an irreversible oxidation wave was observed for the corresponding complexes without *tert*-butyl groups in CuL^1 and $CuL^{1,Me}$ with a significant electrochemical potential shift of 110 mV. The question whether replacement of the *tert*-Bu group in the ortho position of the phenolic moiety by a thiomethyl group can produce a better model of GAO/GLO remains to be clarified.

■ ASSOCIATED CONTENT

Ⓢ Supporting Information. X-ray crystal data in CIF format, EPR spectra, cyclic voltammograms, plots of frontier orbitals, electronic absorption spectra, optimized geometries, and spin-density distribution for both metal complexes and metal-free ligands (or their one-electron oxidized species). The material is available free of charge via the Internet at http://pubs.acs.org.

■ AUTHOR INFORMATION

Corresponding Author

*E-mail: vladimir.arion@univie.ac.at (V.B.A.); peter.rapta@stuba.sk (P.R.); jtelser@roosevelt.edu (J.T.).

■ ACKNOWLEDGMENT

We thank Prof. Brian M. Hoffman (Northwestern University, Evanston, IL) for graciously allowing use of his Q-band EPR instrumentation, which is supported by the NIH (grant HL13531). The financial support of the Science and Technology Assistance Agency (contract no. APVV-0093-07), Slovak Grant Agency VEGA (contract nos. 1/0817/08 and 1/0127/09), Austrian Exchange Service (ÖAD; project no. SK-03), and European Regional Development Fund, Sectoral Operational Program "Increase of Economic Competitiveness", Priority Axis 2 (SOP IEC-A2-O2.1.2-2009-2, ID570, COD SMIS-CSNR: 12473, Contract 129/2010-POLISILMET) is also gratefully acknowledged.

■ REFERENCES

(1) (a) Ito, N.; Phillips, S. E. V.; Stevens, C.; Ogel, Z. B.; McPherson, M. J.; Keen, J. N.; Yadav, K. D. S.; Knowles, P. F. *Nature* **1991**, *350*, 87–90. (b) Ito, N.; Phillips, S. E. V.; Yadav, K. D. S.; Knowles, P. F. *J. Mol. Biol.* **1994**, *238*, 794–814.

(2) (a) Kersten, P. J. *Proc. Natl. Acad. Sci. U.S.A.* **1990**, *87*, 2936–2940. (b) Whittaker, M. M.; Kersten, P. J.; Nakamura, N.; Sanders-Loehr, J.; Schweizer, E. S.; Whittaker, J. W. *J. Biol. Chem.* **1996**, *271*, 681–687. (c) Bork, P.; Doolittle, R. F. *J. Mol. Biol.* **1994**, *236*, 1277–1282.

(3) Goldberg, D. P.; Lippard, S. J. *Adv. Chem. Ser.* **1995**, *246*, 61–81.

(4) Chaudhuri, P.; Wieghardt, K. *Prog. Inorg. Chem.* **2001**, *50*, 151–216.

(5) Jazdzewski, B. A.; Tolman, W. B. *Coord. Chem. Rev.* **2000**, *200—202*, 633–685.

(6) Itoh, S.; Taki, M.; Fukuzumi, S. *Coord. Chem. Rev.* **2000**, *198*, 3–20.

(7) Saint-Aman, E.; Ménage, S.; Pierre, J.-L.; Defrancq, E.; Gellon, G. *New J. Chem.* **1998**, 393–394.

(8) Pratt, R. C.; Stack, T. D. P. *Inorg. Chem.* **2005**, *44*, 2367–2375.

(9) Nairn, A. K.; Archibald, S. J.; Bhalla, R.; Gilbert, B. C.; MacLean, E. J.; Teat, S. J.; Walton, P. H. *Dalton Trans.* **2006**, 172–176.

(10) Bernardo, K.; Leppard, S.; Robert, A.; Commenges, G.; Fahan, F.; Meunier, B. *Inorg. Chem.* **1996**, *35*, 387–396.

(11) Rotthaus, O.; Jarjayes, O.; Philouze, C.; Del Valle, C. P.; Thomas, F. *Dalton Trans.* **2009**, 1792–1800.

(12) Glaser, T.; Heidemeier, M.; Fröhlich, R.; Hildebrandt, P.; Bothe, E.; Bill, E. *Inorg. Chem.* **2005**, *44*, 5467–5482.

(13) Shimazaki, Y.; Yajima, T.; Tani, F.; Karasawa, S.; Fukui, K.; Naruta, Y.; Yamauchi, O. *J. Am. Chem. Soc.* **2007**, *129*, 2559–2568.

(14) Vinck, E.; Murphy, D. M.; Fallis, I. A.; Van Doorslaer, S. *Inorg. Chem.* **2010**, *49*, 2083–2092.

(15) Dos Anjos, A.; Bortoluzzi, A. J.; Szpoganicz, B.; Caro, M. S. B.; Friedermann, G. R.; Mangrich, A. S.; Neves, A. *Inorg. Chim. Acta* **2005**, *358*, 3106–3114.

(16) Shimazaki, Y.; Tani, F.; Fukui, K.; Naruta, Y.; Yamauchi, O. *J. Am. Chem. Soc.* **2003**, *125*, 10512–10513.

(17) Evangelio, E.; Ruiz-Molina, D. *Eur. J. Inorg. Chem.* **2005**, 2957–2971.

(18) (a) Rotthaus, O.; Jarjayes, O.; Thomas, F.; Philouze, C.; Del Valle, C. P.; Saint-Aman, E.; Pierre, J.-L. *Chem.—Eur. J.* **2006**, *12*, 2293–2302. (b) Rotthaus, O.; Thomas, F.; Jarjayes, O.; Philouze, C.; Saint-Aman, E.; Pierre, J.-L. *Chem.—Eur. J.* **2006**, *12*, 6953–6962.

(19) Adams, H.; Bailey, N. A.; Fenton, D. E.; He, Q.; Ohba, M.; Okawa, H. *Inorg. Chim. Acta* **1994**, *215*, 1–3.

(20) Manner, V. W.; Markle, T. F.; Freudenthal, J. H.; Roth, J. P.; Mayer, J. M. *Chem. Commun.* **2008**, 256–258.

(21) Thomas, F.; Jarjayes, O.; Duboc, C.; Philouze, C.; Saint-Aman, E.; Pierre, J.-L. *Dalton Trans.* **2004**, 2662–2669.

(22) Bill, E.; Müller, J.; Weyhermüller, T.; Wieghardt, K. *Inorg. Chem.* **1999**, *38*, 5795–5802.

(23) Freund, M.; Paradies, T. *Ber. Dtsch. Chem. Ges.* **1901**, *33*, 3113.

(24) Neunhoeffer, H.; Weischedel, F. *Liebigs Ann. Chem.* **1971**, *749*, 16–23.

(25) Rudolph, G.; Henry, M. C. *Inorg. Synth.* **1967**, *10*, 74–77.

(26) Werst, M. M.; Davoust, C. E.; Hoffman, B. M. *J. Am. Chem. Soc.* **1991**, *113*, 1533–1538.

(27) *SAINT-Plus*, Version 7.06a; *APEX2*; Bruker-Nonius AXS Inc.: Madison, WI, 2004.

(28) Sheldrick, G. M. *Acta Crystallogr.* **2008**, *A64*, 112.

(29) Johnson, C. K. *Report ORNL-5138*; Oak Ridge National Laboratory: Oak Ridge, TN, 1976.

(30) Frisch, M. J. et al. *Gaussian 03*, Revision D.01; Gaussian, Inc.: Wallingford, CT, 2004. www.gaussian.com (accessed Feb 2011).

(31) Gerbeleu, N. V.; Arion, V. B.; Burgess, J. *Template Synthesis of Macrocyclic Compounds*; Wiley-VCH, Weinheim, Germany, 1999; p 575.

(32) Simonov, Yu. A.; Gerbeleu, N. V.; Bourosh, P. N.; Arion, V. B.; Revenko, M. D.; Pakhopol, V. S.; Malinowsky, T. I. *Dokl. Akad. Nauk SSSR* **1987**, *297*, 608.

(33) Gerbeleu, N. V.; Simonov, Yu. A.; Revenko, M. D.; Arion, V. B.; Pakhopol, V. S.; Bourosh, P. N.; Indrichan, K. M.; Palii, S. P. *Koord. Khim.* **1988**, *14*, 806–812.

(34) Bourosh, P. N.; Simonov, Yu. A.; Arion, V. B.; Sobolev, A. N.; Gerbeleu, N. V.; Pakhopol, V. S. *Kristallografiya* **1989**, *34*, 637–641.

(35) Gerbeleu, N. V.; Arion, V. B.; Simonov, Yu.A.; Bourosh, P. N.; Dvorkin, A. A.; Indrichan, K. M. *Russ. J. Inorg. Chem.* **1990**, *35*, 515–519.

(36) Addison, A. W.; Rao, T. N.; Reedijk, J.; Van Rijn, J.; Verschoor, G. C. *J. Chem. Soc., Dalton Trans.* **1984**, 1349–1356.

(37) Hyde, J. S.; Froncisz, W. *Annu. Rev. Biophys. Bioeng.* **1982**, *11*, 391–417.

(38) Peisach, J.; Blumberg, W. E. *Arch. Biochem. Biophys.* **1974**, *165*, 691–708.

(39) Van Haare, J. A. E. H.; Havinga, E. E.; van Dongen, J. L. J.; Janssen, R. A. J.; Cornil, J.; Bredas, J. L. *Chem.—Eur. J.* **1998**, *4*, 1509–1522.

(40) Alberti, A.; Ballarin, B.; Guerra, M.; Macciantelli, D.; Mucci, A.; Parenti, F.; Schenetti, L.; Seeber, R.; Zanardi, C. *ChemPhysChem.* **2003**, *4*, 1216–1225.

(41) Wang, Y. D.; DuBois, J. L.; Hedman, B.; Hodgson, K. O.; Stack, T. D. P. *Science* **1998**, *279*, 537–540.

(42) Tarábek, J.; Rapta, P.; Kalbác, M.; Dunsch, L. *Anal. Chem.* **2004**, *76*, 5918–5923.

(43) Belford, R. L. *QPOWA*; University of Illinois, Urbana, IL. Modified by Telser, J. See: Belford, R. L.; Nilges, M. J. In , *EPR Symposium*, 21 Rocky Mountain Conference, Denver, CO, August, 1979.

(44) McGarvey, B. R. *Can. J. Chem.* **1975**, *53*, 2498–2511.

(45) Nickel complexes with very non-innocent ligands, such as bis(dithiolene) ligands, can be described formally as Ni(III) but are actually Ni(II) with ligand-centered radicals. See: Ray, K.; Weyhermueller, T.; Neese, F.; Wieghardt, K. *Inorg. Chem.* **2005**, *44*, 5345–5360.

(46) Wieghardt, K.; Walz, W.; Nuber, B.; Weiss, J.; Ozarowski, A.; Statemeier, H.; Reinen, D. *Inorg. Chem.* **1986**, *25*, 1650–1654.

(47) Gore, E. S.; Busch, D. H. *Inorg. Chem.* **1973**, *12*, 1–3.

(48) Jaun, B. *Helv. Chim. Acta* **1990**, *73*, 2209–2217.

(49) Weltner, W., Jr. *Magnetic Atoms and Molecules*; Dover: New York, 1989; Chapter 3.

(50) Gerbeleu, N. V.; Palanciuc, S. S.; Simonov, Yu.A.; Dvorkin, A. A.; Reetz, M. T.; Arion, V. B.; Töllner, K. *Polyhedron* **1995**, *14*, 521–527.

(51) Halcrow, M. A.; Chia, L. M. L.; McInnes, E. J. L.; Yellowlees, L. J.; Mabbs, F. E.; Davies, J. E. *Chem. Commun.* **1998**, 2465–2466.

(52) Itoh, S.; Taki, M.; Takayama, S.; Nagatomo, S.; Kitagawa, T.; Sakurada, N.; Arakawa, S.; Fukuzumi, S. *Angew. Chem., Int. Ed. Engl.* **1999**, *38*, 2774–2776.

(53) Itoh, S.; Takayama, S.; Arakawa, R.; Furuta, A.; Komatsu, M.; Ishida, S.; Takamuku, S.; Fukuzumi, S. *Inorg. Chem.* **1997**, *36*, 1407–1416.